Ultramicroscopy 245 (2023) 113664

Contents lists available at ScienceDirect

Ultramicroscopy

journal homepage: www.elsevier.com/locate/ultramic

Coherent electron Compton scattering and the non-diagonal electron momentum density of solids

B.G. Mendis

Department of Physics, Durham University, South Road, Durham DH1 3LE, UK

ARTICLE INFO

Keywords:
Coherent Compton scattering
Electron density matrix
Mixed dynamic form factor
Electron energy loss spectroscopy

ABSTRACT

Experimental techniques that probe the electronic structure of crystalline solids are vital for exploring novel condensed matter phenomena. In coherent Compton scattering the Compton signal due to interference of an incident and Bragg diffracted beam is measured. This gives the projected, non-diagonal electron momentum density of the solid, a quantity that is sensitive to both the amplitude and phase of the electron wavefunction. Here coherent electron Compton scattering is demonstrated using electron energy loss spectroscopy in the transmission electron microscope. The technique has several advantages over coherent X-ray Compton scattering, such as a superior spatial resolution and the use of smaller specimens to generate Bragg beams of sufficient intensity. The conditions for a directly interpretable coherent electron Compton signal are established. Results are presented for the projected, non-diagonal electron momentum density for silicon under 004 and $\bar{2}20$ Bragg beam set ups.

1. Introduction

Compton inelastic scattering measures the electron momentum density of a solid projected along the scattering vector direction, i.e. the so-called $J(p_z)$ function. The material electronic structure is analysed in reciprocal space, to provide information on any anisotropy in electron bonding, magnetism and phase transitions [1]. Photon-based Compton scattering using X-ray or γ-ray radiation are well established techniques, but its application to high energy electron beams and electron energy loss spectroscopy (EELS) has been rather limited [2–10]. This has largely been due to artefacts introduced by Bragg scattering in a crystalline specimen. Both the unscattered and Bragg diffracted beams can undergo Compton scattering, although there will be a difference in the scattering vector (magnitude and/or direction) for each beam. The mapping of $J(p_z)$ to the EELS spectrum is a function of the scattering vector magnitude, such that Compton profiles at larger scattering angles appear more broadened and are shifted to higher energy losses [10]. Furthermore, if the scattering vectors are not crystallographically equivalent the Compton profile shapes could be different due to anisotropy in $J(p_z)$, although this is a comparatively minor effect [1]. Since the overall Compton signal is a superposition of the contribution from all beams, the EELS measurement is not an accurate representation of $J(p_z)$ when the sample is strongly diffracting. However, a multislice-based method has recently been proposed for simulating electron Compton spectra, taking into account diffraction of the high energy electron beam both before and after the Compton scattering event [11]. Using multislice it is possible to invert the experimental measurement and extract an 'isotropic' $J(p_z)$ that is averaged over the different scattering vectors. The isotropic $J(p_z)$ is largely free of the distortions due to diffraction.

Although diffraction is generally undesirable there are special cases where it can provide useful information beyond a standard Compton measurement. The technique is called 'coherent' Compton scattering [12] and exploits the well-defined phase relationship between the elastically scattered electrons. Interference between the Bragg beams can therefore also contribute to the Compton signal. The mixed dynamic form factor (MDFF) quantifies the interference contribution to the inelastic scattering cross-section [13–14]. It has previously been used to calculate the core-loss EELS signal from focused electron beams [15], electron magnetic circular dichroism (EMCD) in magnetic materials [16], as well as mapping atomic orbitals [17]. In Compton scattering the $J(p_z)$ function and MDFF respectively sample the diagonal and non-diagonal terms of the electron density matrix in reciprocal space [12]. Non-diagonal terms depend on both the amplitude and phase of the electron wavefunction, and are therefore a more sensitive measure of the electronic structure.

The MDFF in electron Compton scattering has previously been investigated by Schattschneider and co-workers [3-4,6-7]. Here we build on this earlier work to establish coherent electron Compton

E-mail address: b.g.mendis@durham.ac.uk.

https://doi.org/10.1016/j.ultramic.2022.113664
Received 26 September 2022; Received in revised form 28 November 2022; Accepted 17 December 2022
Available online 18 December 2022

scattering as a robust EELS technique. Compared to X-rays, high energy electrons provide several benefits for coherent Compton scattering measurements. The first is the higher spatial resolution of a transmission electron microscope, i.e. data can be acquired from specimen regions ~100 nm in size or smaller. The second advantage is the strong Bragg diffraction, which renders the (crystalline) specimen an efficient beam splitter for the high energy electrons. Therefore, Bragg beams of sufficient intensity can be obtained from much thinner crystals, a key requirement for materials that are hard to fabricate in single crystal form, as well as 2D materials that are intrinsically thin. In this paper, the MDFF cross-section for Compton scattering is derived theoretically, and the conditions for the MDFF to be directly interpretable are identified. Experimental data is presented for silicon, which has been extensively studied using electron Compton scattering [3-4,6-7,11], and is therefore an ideal test specimen. Two-beam diffraction conditions for the 004 and $\bar{2}20$ reflections are used to extract the projected, non-diagonal matrix elements of the electron momentum density.

2. Methods

2.1. Experimental

Electron Compton measurements were carried out in a JEOL 2100F FEG TEM operating at 200 kV. The sample was a [110]-oriented silicon wafer that was thinned using argon ion-beam milling. A Gatan Tridiem EELS spectrometer was used for recording the Compton spectra in image mode. The specimen thickness, estimated from the thickness to EELS inelastic mean free path ratio, was ~70 nm. Two-beam centred dark field illumination, where either the 004 or $\bar{2}20$ Bragg beam is strongly excited, is used for coherent Compton scattering. Diffraction of both the incoming and outgoing electron beams are important in Compton measurements, the latter being determined by the EELS aperture [11], which is positioned along the electron optic axis. The sample is therefore tilted away from the [110] zone axis along the relevant Kikuchi band to minimise diffraction of the outgoing beam. The tilt angles were 159 mrad and 144 mrad for the 004 and $\bar{2}20$ measurements respectively. The diffraction pattern for the former is shown in Fig. 1a. A logarithmic intensity scale is used to bring out all features in the diffraction pattern; the linear intensity scale diffraction patterns can be found in the Supplementary Material.

Compton spectra were acquired under Bragg, as well as both positive and negative deviation parameter (s_g) settings; example diffraction patterns are shown in Fig. 1b to 1d. The EELS aperture is at the symmetry orientation of the Kikuchi band (see annotation in Fig. 1b). The EELS collection semi-angle is limited by the 5.3 mrad objective aperture used for centred dark-field imaging. The Compton scattering vector magnitude for the 000 and Bragg beam are exactly equal for $s_g = 0$, and approximately equal for the small deviation parameters used here. Furthermore, there is no anisotropy in $J(p_z)$ for the 000 beam and $\mathbf{g} =$ 004 or $\bar{2}20$ reflections, due to the crystal symmetry of silicon [3]. The Compton scattering angle is 49 mrad and 46 mrad for the 004 and $\bar{2}20$ measurements respectively.

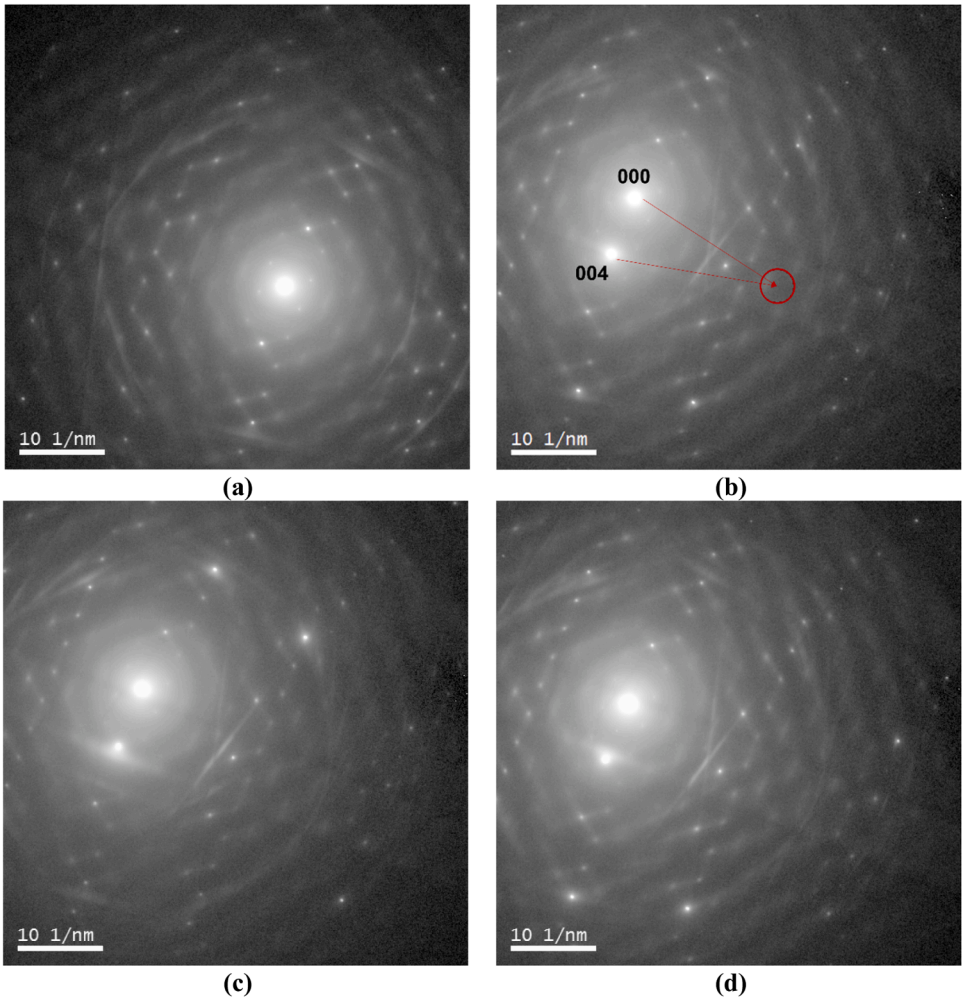

Fig. 1. (a) Electron diffraction pattern for the silicon sample in the 004 symmetry orientation, tilted 159 mrad away from the [110] zone axis. The incident electron beam is parallel to the optic axis. Centred dark-field electron diffraction patterns for 004 Bragg, positive and negative deviation parameter are shown in (b), (c) and (d) respectively. The red circle in (b) indicates the position and size of the EELS aperture (the EELS spectrometer is along the optic axis). The two arrows represent Compton scattering vectors for the 000 and 004 reflections. Diffraction pattern intensities are displayed on a logarithmic scale.

2.2. Multislice simulation

Compton spectra were simulated using the double multislice method described in [11]. The principle of this method is illustrated schematically in Fig. 2a, which shows a Compton scattering event at the real space position P. Elastic propagation of the incident wavefunction Ψ_{inc} to the specimen depth d is performed using multislice for an inclined electron beam [18]. Each Bragg beam in the forward multislice diffraction pattern is a potential source of Compton scattering, which can take place in many directions (Fig. 2a). Following the Compton event, the high energy electron can undergo further elastic scattering on its way to the specimen exit surface. However, only the far-field exit wavefunction Ψ_{exit} in the direction of the EELS aperture is detected. Applying principle of reciprocity [19] the wavevector of Ψ_{exit} is reversed, and multislice propagated to the specimen depth where Compton scattering takes place. Fourier transforming this reverse multislice wavefunction reveals the Bragg diffraction vectors for elastic scattering of the outgoing high energy electron. Fig. 2b illustrates the process in reciprocal space. The Bragg beam $\mathbf{g}_1$ in the forward multislice diffraction pattern is a source of Compton scattering. $\mathbf{g}_2$ is a Bragg vector in the reverse multislice diffraction pattern; the high energy electron can be scattered along this vector while exiting the specimen, meaning that Compton scattering along the vector $\mathbf{q}$ will be detected by the EELS aperture (Fig. 2b). The measured Compton signal is proportional to $[I(\mathbf{g}_1)I(\mathbf{g}_2)/q^4]$, where $I(\mathbf{g}_1)$, $I(\mathbf{g}_2)$ are the intensities of the $\mathbf{g}_1$ and $\mathbf{g}_2$ Bragg beams in the forward and reverse multislice diffraction patterns at the specimen depth d for Compton scattering, and q is the magnitude of $\mathbf{q}$ [11]. A mathematical justification for this expression is given in Section 3. The EELS Compton profile shape is governed by $J(p_z)$, the number of solid-state electrons with momentum component p_z parallel to the scattering vector $\mathbf{q}$. The energy loss $\Delta E(p_z)$ corresponding to momentum p_z is calculated using the following equations [10]:

$$\Delta E(p_z) = \Delta E_p + \delta E(p_z) \tag{1a}$$

$$\Delta E_p = 2\sin^2\frac{\varphi}{2}\left(2T + \frac{T^2}{m_0c^2}\right) \tag{1b}$$

$$\delta E(p_z) = -p_z\sqrt{\frac{2\Delta E_p}{m_0}} \tag{1c}$$

where ΔE_p is the energy loss for the Compton profile maximum and $\delta E(p_z)$ is the Doppler broadening term. φ is the Compton scattering angle, T is the incident electron kinetic energy and m_0c^2 is the electron rest mass energy. The EELS Compton signal at energy loss $\Delta E(p_z)$ is proportional to $J(p_z)/\sqrt{\Delta E_p}$. The normalisation constant $(\Delta E_p)^{-1/2}$ satisfies the sum rule for Compton scattering, i.e. the area under the Compton profile is fixed by the number of solid-state electrons undergoing Compton scattering. As an example, there are 12 electrons per silicon atom for Compton energy losses between the Si L and K-edges. The origin of the normalisation constant is clear from Eq. (1c), where there is a linear relationship between momentum p_z and Compton profile broadening. The EELS Compton spectrum $I(E)$ is therefore [11]:

$$I(E) = \sum_{d,\mathbf{g}_1,\mathbf{g}_2,p_z} \frac{I(\mathbf{g}_1)I(\mathbf{g}_2)}{q^4}\left[\frac{J(p_z)}{\sqrt{\Delta E_p}}\right]\delta\big(E - \Delta E(p_z)\big) \tag{2}$$

The summation over d includes Compton scattering from all depths within the specimen. The delta function is equal to unity if the energy loss $E = \Delta E(p_z)$ and zero otherwise. Eq. (2) is valid to within a proportionality constant, which can be omitted, since we are not interested in absolute intensities. Note that Eq. (2) only includes the direct Compton scattering contributions from the transmitted and Bragg diffracted beams. In principle, it is possible to extend the general methodology to also include coherent Compton scattering (see Eq. 16 below), but this requires the projected non-diagonal terms in the electron momentum density matrix, which are generally unknown (in fact, some of the terms are experimentally measured in this work).

The multislice supercell had lateral dimensions of 76.02 × 76.02 Å and was sampled using 1024 × 1024 pixels. Many of the simulation parameters were obtained directly from experiment, such as the incident electron beam energy (200 kV) and wavevector, specimen thickness (70 nm) and orientation, as well as EELS collection angles. Strictly speaking, the finite sized EELS aperture will detect multiple wavevectors for the outgoing electron beams. Instead of simulating all of them via separate reverse multislice calculations, it is computationally more efficient to simulate only the wavevector corresponding to the centre of the EELS aperture and vary the Compton scattering vector $\mathbf{q}$ to cover all EELS collection angles. This approach assumes the reverse multislice calculation is weakly dependent on the exit electron wavevector and is therefore only valid for small EELS apertures. The EELS collection semi-angle in our measurements is only 5.3 mrad, and the simulation results agree well with experiment (see Fig. 3), which justifies the use of such an approximation. The supercell was divided into 1.92 Å thick slices along the electron optic axis direction. Kirkland's [20] atom scattering factors were used to calculate the projected atom potential within a given slice. Frozen phonons were calculated within the Einstein approximation by applying a 0.078 Å rms displacement randomly to individual silicon

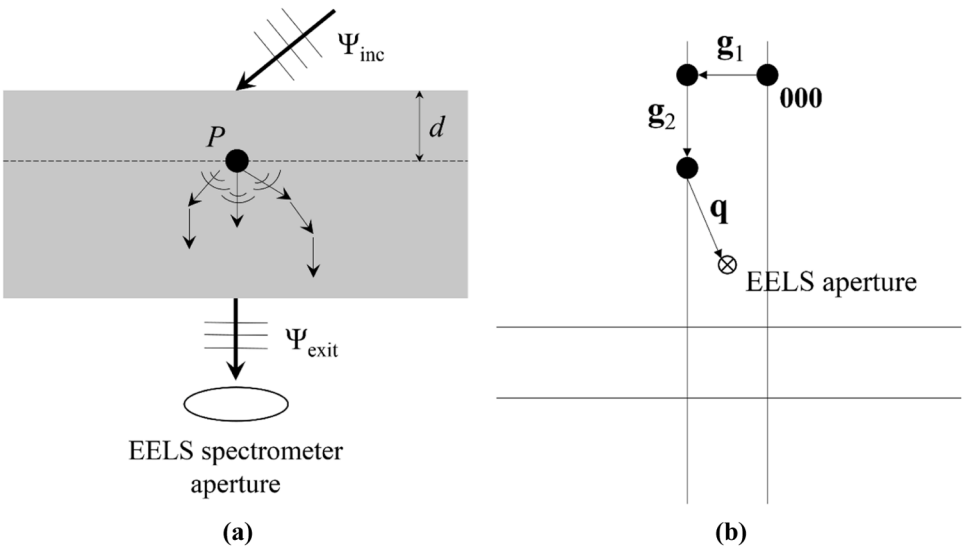

Fig. 2. (a) Schematic of Compton scattering. The incident electron wavefunction Ψ_{inc} is Compton scattered at point P (depth d) within the sample in many directions. The outgoing electrons can undergo further elastic scattering, but only the electron wavefunction Ψ_{exit} in the direction of the EELS aperture is detected. (b) An illustration of the same process in reciprocal space. The $\mathbf{g}_1$ Bragg beam is Compton scattered at a given depth, followed by further elastic scattering of the outgoing beam by reciprocal vector $\mathbf{g}_2$. The EELS aperture detects the Compton scattering along $\mathbf{q}$.

atoms. An experimentally measured $J(p_z)$ for silicon [11] was used to calculate the electron Compton spectrum according to Eq. (2). Compton spectra from 20 different frozen phonon configurations were summed to give a statistically significant result.

3. Compton scattering and electron momentum density

A second quantisation derivation of the dynamic form factor for Compton scattering is presented in Schattschneider et al. [21], while the MDFF is derived in Exner and Schattschneider [7]. In this section we discuss a slightly different derivation for the MDFF, which reveals some useful insights into coherent electron Compton scattering. Starting with the Fermi Golden rule, the double differential inelastic scattering cross-section (σ) is given by [22]:

$$\frac{\partial^2\sigma}{\partial\Omega\partial E}\propto\sum_{f,N}|\langle b|V(\mathbf{r},\mathbf{r}_N)|a\rangle|^2\delta(E-E_f+E_i) \tag{3}$$

where Ω is the scattering solid angle and E is the energy loss. $V(\mathbf{r},\mathbf{r}_N)$ is the interaction potential between the incident high energy electron (position vector $\mathbf{r}$) and solid-state electrons (position vector $\mathbf{r}_N$ for N^{th} electron) in the Born-Oppenheimer approximation. $|a\rangle=|\psi_i\rangle|i\rangle$ is the initial state of the system, where $|\psi_i\rangle$ is the incident electron wavefunction before Compton scattering and $|i\rangle$ is the ground state of the solid, which has energy E_i. Similarly, $|b\rangle=|\psi_e\rangle|f\rangle$ is the final state after Compton scattering, with $|f\rangle$ being the solid excited state (energy E_f). The exit electron wavefunction $|\psi_e\rangle$ must be detected by the EELS spectrometer and is therefore determined by the principle of reciprocity [19]. The summation in Eq. (3) is over all excited states and solid-state electrons, while the delta function ensures energy conservation during inelastic scattering.

It is convenient to express the electron wavefunctions as inverse Fourier transforms:

$$|\psi_i\rangle=\int\phi_i(\mathbf{k}_i)e^{2\pi i\mathbf{k}_i\cdot\mathbf{r}}d\mathbf{k}_i \tag{4a}$$

$$|\psi_e\rangle=\int\phi_e(\mathbf{k}_e)e^{2\pi i\mathbf{k}_e\cdot\mathbf{r}}d\mathbf{k}_e \tag{4b}$$

where $\mathbf{k}_i$ and $\mathbf{k}_e$ are reciprocal vectors and the ϕ's represent Fourier coefficients. Using the relationship [22]:

$$\int V(\mathbf{r},\mathbf{r}_N)e^{2\pi i(\mathbf{k}_i-\mathbf{k}_e)\cdot\mathbf{r}}d\mathbf{r}\propto\frac{e^{-2\pi i\mathbf{q}\cdot\mathbf{r}_N}}{q^2} \tag{5}$$

where $\mathbf{q}=\mathbf{k}_e-\mathbf{k}_i$ is a scattering vector, the square matrix element in Eq. (3) becomes:

$$|\langle b|V(\mathbf{r},\mathbf{r}_N)|a\rangle|^2\propto\int\frac{\phi_e^*(\mathbf{k}_e)\phi_e(\mathbf{k}'_e)\phi_i^*(\mathbf{k}'_i)\phi_i(\mathbf{k}_i)}{(qq')^2}\times \langle i|e^{2\pi i\mathbf{q}'\cdot\mathbf{r}_N}|f\rangle\langle f|e^{-2\pi i\mathbf{q}\cdot\mathbf{r}_N}|i\rangle d\mathbf{k}_i d\mathbf{k}'_i d\mathbf{k}_e d\mathbf{k}'_e \tag{6}$$

where an asterisk denotes the complex conjugate and $\mathbf{q}'=\mathbf{k}'_e-\mathbf{k}'_i$ is a second scattering vector. Since $E=\hbar\omega$ ($\hbar$ is Planck's reduced constant and ω is angular frequency) the delta function in Eq. (3) can be expressed in the alternative form [22]:

$$\delta(E-E_f+E_i)=\frac{1}{2\pi}\int e^{i(E_f-E_i)t}e^{-i(\hbar\omega)t}dt \tag{7}$$

Substituting Eqs. (6) and (7) in (3) gives:

$$\frac{\partial^2\sigma}{\partial\Omega\partial E}\propto\sum_{f,N}\int\frac{\phi_e^*(\mathbf{k}_e)\phi_e(\mathbf{k}'_e)\phi_i^*(\mathbf{k}'_i)\phi_i(\mathbf{k}_i)}{(qq')^2}\times \langle i|e^{-iE_it}e^{2\pi i\mathbf{q}'\cdot\mathbf{r}_N}e^{iE_ft}|f\rangle\langle f|e^{-2\pi i\mathbf{q}\cdot\mathbf{r}_N}|i\rangle e^{-i(\hbar\omega)t}dtd\mathbf{k}_i d\mathbf{k}'_i d\mathbf{k}_e d\mathbf{k}'_e \tag{8}$$

Using the equations $e^{-i\widehat{H}t}|i\rangle=e^{-iE_it}|i\rangle$ and $e^{i\widehat{H}t}|f\rangle=e^{iE_ft}|f\rangle$, derived from $\widehat{H}|i\rangle=E_i|i\rangle$ and $\widehat{H}|f\rangle=E_f|f\rangle$ respectively, and the completeness relation $\sum_f|f\rangle\langle f|=\widehat{I}$, where $\widehat{H},\widehat{I}$ are the Hamiltonian for the solid and identity operators respectively, Eq. (8) simplifies to:

$$\frac{\partial^2\sigma}{\partial\Omega\partial E}\propto\int\frac{\phi_e^*(\mathbf{k}_e)\phi_e(\mathbf{k}'_e)\phi_i^*(\mathbf{k}'_i)\phi_i(\mathbf{k}_i)}{(qq')^2}\times \left[\sum_N\langle i|e^{-i\widehat{H}t}e^{2\pi i\mathbf{q}'\cdot\mathbf{r}_N}e^{i\widehat{H}t}e^{-2\pi i\mathbf{q}\cdot\mathbf{r}_N}|i\rangle\right]e^{-i(\hbar\omega)t}dtd\mathbf{k}_i d\mathbf{k}'_i d\mathbf{k}_e d\mathbf{k}'_e \tag{9}$$

The Hamiltonian is $\widehat{H}=\widehat{H}_o+V_o$, where $\widehat{H}_o$ is the kinetic energy operator and V_o is the electrostatic potential for the solid. In the impulse approximation it is assumed that the scattering time t is negligible, a condition that is satisfied for large momentum transfers and energy loss significantly higher than the binding energy of the solid-state electron undergoing inelastic scattering. The accuracy of the impulse approximation is discussed in [23]. Assuming second and higher order terms in time can be neglected results in the following approximation:

$$e^{i\widehat{H}t}\approx e^{i\widehat{H}_ot}e^{iV_ot} \tag{10}$$

Eq. (10) can be substituted in the matrix element of Eq. (9) to give :

$$\begin{aligned}&\langle i|e^{-i\widehat{H}t}e^{2\pi i\mathbf{q}'\cdot\mathbf{r}_N}e^{i\widehat{H}t}e^{-2\pi i\mathbf{q}\cdot\mathbf{r}_N}|i\rangle\approx\langle i|e^{-i\widehat{H}_ot}e^{-iV_ot}e^{2\pi i\mathbf{q}'\cdot\mathbf{r}_N}e^{i\widehat{H}_ot}e^{iV_ot}e^{-2\pi i\mathbf{q}\cdot\mathbf{r}_N}|i\rangle\\&\approx\langle i|e^{-i\widehat{H}_ot}(1-iV_ot)e^{2\pi i\mathbf{q}'\cdot\mathbf{r}_N}e^{i\widehat{H}_ot}(1+iV_ot)e^{-2\pi i\mathbf{q}\cdot\mathbf{r}_N}|i\rangle\\&\approx\langle i|e^{-i\widehat{H}_ot}e^{2\pi i\mathbf{q}'\cdot\mathbf{r}_N}e^{i\widehat{H}_ot}e^{-2\pi i\mathbf{q}\cdot\mathbf{r}_N}|i\rangle\end{aligned} \tag{11}$$

where second and higher order terms in time have again been ignored. Within the impulse approximation the potential is therefore absent from the scattering cross-section, implying that the solid-state electrons effectively behave as free particles. This is because the collision time is too short for neighbouring solid-state electrons and nuclei to re-arrange during inelastic scattering, which results in a constant potential over the relevant time scales. Compare this with core loss EELS edges, where the collision time can be long enough for core hole screening [24].

Following [7] the identity operator, expressed via a momentum basis set, is inserted multiple times in Eq. (11), i.e. :

$$\begin{aligned}&\sum_N\langle i|e^{-i\widehat{H}_ot}e^{2\pi i\mathbf{q}'\cdot\mathbf{r}_N}e^{i\widehat{H}_ot}e^{-2\pi i\mathbf{q}\cdot\mathbf{r}_N}|i\rangle\\&=\sum_{\mathbf{p},\mathbf{p}',\mathbf{p}''}\langle i|\mathbf{p}\rangle\left\langle\mathbf{p}\left|e^{-i\widehat{H}_ot}\left(\sum_N e^{2\pi i\mathbf{q}'\cdot\mathbf{r}_N}\right)\right|\mathbf{p}'\right\rangle\left\langle\mathbf{p}'\left|e^{i\widehat{H}_ot}\left(\sum_N e^{-2\pi i\mathbf{q}\cdot\mathbf{r}_N}\right)\right|\mathbf{p}''\right\rangle\langle\mathbf{p}''|i\rangle\end{aligned} \tag{12}$$

where $|\mathbf{p}\rangle$, $|\mathbf{p}'\rangle$ and $|\mathbf{p}''\rangle$ are dummy variables for the momentum basis set and $\sum_{\mathbf{p}}|\mathbf{p}\rangle\langle\mathbf{p}|=\widehat{I}$ etc. The matrix elements in Eq. (12) are evaluated as follows:

$$\begin{aligned}\left\langle\mathbf{p}\left|e_o^{-i\widehat{H}}t\left(\sum_N e^{2\pi i\mathbf{q}'\cdot\mathbf{r}_N}\right)\right|\mathbf{p}'\right\rangle&=\langle\mathbf{p}|1-i\widehat{H}_ot+\ldots|\mathbf{p}'+\mathbf{q}'\rangle\\&=\delta(\mathbf{p}-\mathbf{p}'-\mathbf{q}')\left[1-i\frac{h^2(\mathbf{p}'+\mathbf{q}')^2}{2m}t+\cdots\right]\\&=\delta(\mathbf{p}-\mathbf{p}'-\mathbf{q}')e^{-ih^2(\mathbf{p}'+\mathbf{q}')^2t/2m}\end{aligned} \tag{13}$$

where we have made use of the orthogonality of eigenstates and the fact that for a free electron $\widehat{H}_o|\mathbf{p}'+\mathbf{q}'\rangle=\frac{h^2(\mathbf{p}'+\mathbf{q}')^2}{2m}|\mathbf{p}'+\mathbf{q}'\rangle$. Eq. (12) is then :

$$\sum_N \langle i|e^{-i\widehat{H}_o t}e^{2\pi i\mathbf{q}'\cdot\mathbf{r}_N}e^{i\widehat{H}_o t}e^{-2\pi i\mathbf{q}\cdot\mathbf{r}_N}|i\rangle = \sum_{\mathbf{p},\mathbf{p}',\mathbf{p}''}\langle i|\mathbf{p}\rangle\langle\mathbf{p}''|i\rangle\delta(\mathbf{p}-\mathbf{p}'-\mathbf{q}')\delta(\mathbf{p}'-\mathbf{p}''+\mathbf{q})e^{-ih^2(\mathbf{p}'+\mathbf{q}')^2t/2m}e^{ih^2(\mathbf{p}''-\mathbf{q})^2t/2m} \tag{14}$$

A necessary condition for the MDFF of a perfect crystal to be non-zero is that $\mathbf{q}' - \mathbf{q} = \mathbf{g}$, where $\mathbf{g}$ is a reciprocal lattice vector [14]. Therefore, Eq. (14) simplifies to:

$$\sum_N \langle i|e^{-i\widehat{H}_o t}e^{2\pi i\mathbf{q}'\cdot\mathbf{r}_N}e^{i\widehat{H}_o t}e^{-2\pi i\mathbf{q}\cdot\mathbf{r}_N}|i\rangle = \sum_{\mathbf{p}''}\langle i|\mathbf{p}''+\mathbf{g}\rangle\langle\mathbf{p}''|i\rangle e^{-ih^2(\mathbf{p}''+\mathbf{g})^2t/2m}e^{ih^2(\mathbf{p}''-\mathbf{q})^2t/2m} \tag{15}$$

Substituting in Eq. (9) and evaluating the time integral gives:

$$\frac{\partial^2\sigma}{\partial\Omega\partial E}\propto\int\frac{\phi_e^*(\mathbf{k}_e)\phi_e(\mathbf{k}'_e)\phi_i^*(\mathbf{k}'_i)\phi_i(\mathbf{k}_i)}{(qq')^2}\times \left[\sum_{\mathbf{p}''}\langle i|\mathbf{p}''+\mathbf{g}\rangle\langle\mathbf{p}''|i\rangle\delta\left(\hbar\omega-\frac{h^2(q^2-g^2-2\mathbf{p}''\cdot\mathbf{q}')}{2m}\right)\right]d\mathbf{k}_i d\mathbf{k}'_i d\mathbf{k}_e d\mathbf{k}'_e \tag{16}$$

In the independent electron approximation, the electron wavefunction for the solid satisfies Bloch's theorem [25]:

$$\psi^{(j\mathbf{k})}(\mathbf{x}) = \sum_{\mathbf{g}}\Psi_{\mathbf{g}}^{(j)}(\mathbf{k})e^{2\pi i(\mathbf{k}+\mathbf{g})\cdot\mathbf{x}} \tag{17}$$

where $\psi^{(j\mathbf{k})}$ is the Bloch wavefunction for the j^{th}-band at wavevector $\mathbf{k}$. $\Psi_{\mathbf{g}}^{(j)}(\mathbf{k})$ are the corresponding Bloch coefficients and $\mathbf{x}$ is the position vector of the independent electron. Evaluating the square bracket term in Eq. (16) using Bloch wavefunctions gives:

$$\frac{\partial^2\sigma}{\partial\Omega\partial E}\propto\int\frac{\phi_e^*(\mathbf{k}_e)\phi_e(\mathbf{k}'_e)\phi_i^*(\mathbf{k}'_i)\phi_i(\mathbf{k}_i)}{(qq')^2}\times \left(\sum_{\mathbf{p}_o,\,j'}\left[\Psi_{\mathbf{g}}^{(j')}(\mathbf{p}_o)\right]^*\Psi_0^{(j')}(\mathbf{p}_o)\right)d\mathbf{k}_i d\mathbf{k}'_i d\mathbf{k}_e d\mathbf{k}'_e \tag{18}$$

where $\mathbf{p}_o$ is any vector $\mathbf{p}''$ that satisfies the delta function in Eq. (16) for a given energy loss $\hbar\omega$. It is clear that all such $\mathbf{p}_o$ vectors must have a constant projection along $\mathbf{q}'$. The summation in Eq. (18) is the MDFF for Compton scattering. j' are Bloch bands that have electron binding energies smaller than $\hbar\omega$. More tightly bound Bloch bands cannot undergo Compton scattering due to energy conservation, and must therefore be excluded from the summation. First consider the special case of direct scattering, where $\mathbf{k}_i = \mathbf{k}'_i$ and $\mathbf{k}_e = \mathbf{k}'_e$, so that $\mathbf{q} = \mathbf{q}'$ and $\mathbf{g} = 0$. The summation pre-factor in Eq. (18) is then $|\phi_i(\mathbf{k}_i)|^2|\phi_e(\mathbf{k}_e)|^2/q^4$; this is exactly the term used for calculating the direct scattering intensity in a multislice simulation [11]. The MDFF simplifies to the dynamic form factor, which has the form:

$$\sum_{\mathbf{p}_o,\,j'}\left|\Psi_0^{(j')}(\mathbf{p}_o)\right|^2 \tag{19}$$

The summand is proportional to the number of electrons occupying band j' with wavevector $\mathbf{p}_o$; see Eq. (17). Therefore, Eq. (19) is equivalent to the projected electron momentum density $J(p_z)$.

Next consider the MDFF where $\mathbf{g} \neq \mathbf{0}$. Since Bloch states are orthonormal the following property is valid at any given wavevector $\mathbf{p}_o$ [26]:

$$\sum_{\text{all }j}\left[\Psi_{\mathbf{g}\neq\mathbf{0}}^{(j)}(\mathbf{p}_o)\right]^*\Psi_0^{(j)}(\mathbf{p}_o) = 0 \tag{20}$$

where j includes all Bloch bands, whether they be occupied or unoccupied. The only difference between Eq. (20) and the MDFF is in the number of Bloch bands being summed. The $\Psi_{\mathbf{g}}^{(j)}(\mathbf{p}_o)$ coefficients will in general be larger for the more localised core electrons; the left hand side of Eq. (20) should therefore approach zero after only a few j bands, especially for large $|\mathbf{g}|$. Hence if all electrons participate in Compton scattering the MDFF and coherent scattering cross-section is expected to be small. However, the energy loss in a typical EELS measurement rarely exceeds 1 keV, so that the high binding energy core electrons will not always contribute to electron Compton scattering. In such cases the MDFF cannot be approximated with Eq. (20), and coherent scattering can therefore be non-negligible. Nevertheless, coherent scattering will be weaker for low atomic number solids and large $|\mathbf{g}|$, due to smaller $\Psi_{\mathbf{g}}^{(j)}(\mathbf{p}_o)$ coefficients. This is evident in the numerical results presented in [7] for L and M-shell electrons in silicon. In particular, the MDFF decreased monotonically with $|\mathbf{g}|$; see Fig. 3 in reference [7].

4. Experimental results and discussion

Fig. 3a shows the two-beam , $\mathbf{g} = 004$ EELS Compton spectra acquired under Bragg as well as positive ($s_{\mathbf{g}} = 2.2 \pm 0.1 \times 10^{-2}$ nm^{-1}) and negative ($s_{\mathbf{g}} = -1.7 \pm 0.1 \times 10^{-2}$ nm^{-1}) deviation parameter illumination conditions (the deviation parameters were calculated from the diffraction patterns [27]). The integrated intensity of the Si L-edge region (i.e. 115-175 eV) is normalised for a direct comparison. The relative intensity of the Compton profile increases from negative to positive deviation parameter, and the peak maximum shifts to higher energy losses. For example, the Compton peak maximum is at ~648 eV and 668 eV for negative and positive deviation parameters respectively. Fig. 3b plots the difference between the normalised positive and negative deviation parameter spectra. The difference spectrum peaks at ~700 eV, and the integrated intensity is approximately half that of the background subtracted, Compton profile at negative deviation parameter. The Compton spectrum therefore changes significantly with deviation parameter. The changes are potentially due to direct and indirect scattering contributions, the latter representing the coherent signal due to beam interference.

First consider direct scattering. The diffraction patterns in Fig. 1 confirm the illumination to be effectively two-beam, while there is very little Bragg diffraction of the electron beam exiting the specimen in the direction of the EELS spectrometer (Fig. 1a; see also Supplementary Material for a more detailed analysis of the diffraction patterns). The diffraction conditions can therefore be described as '2 beams in, 1 beam out' [7]. Assuming a point EELS aperture, the Compton scattering vector magnitude q will then be larger for the 000 beam at positive deviation parameter compared to negative deviation parameter (see Fig. 1b for the scattering geometry). The trend is opposite for the Bragg beam, although it is reasonable to focus on the 000 beam, since it has the higher intensity (Fig. 1b-d) and should therefore produce a stronger Compton signal. The larger q at positive deviation parameter will shift the Compton peak to higher energy loss and decrease the signal due to the q^{-4} term in the direct scattering cross-section (Eq. 2). However, since q is already large the fractional change in q due to deviation parameter is relatively small

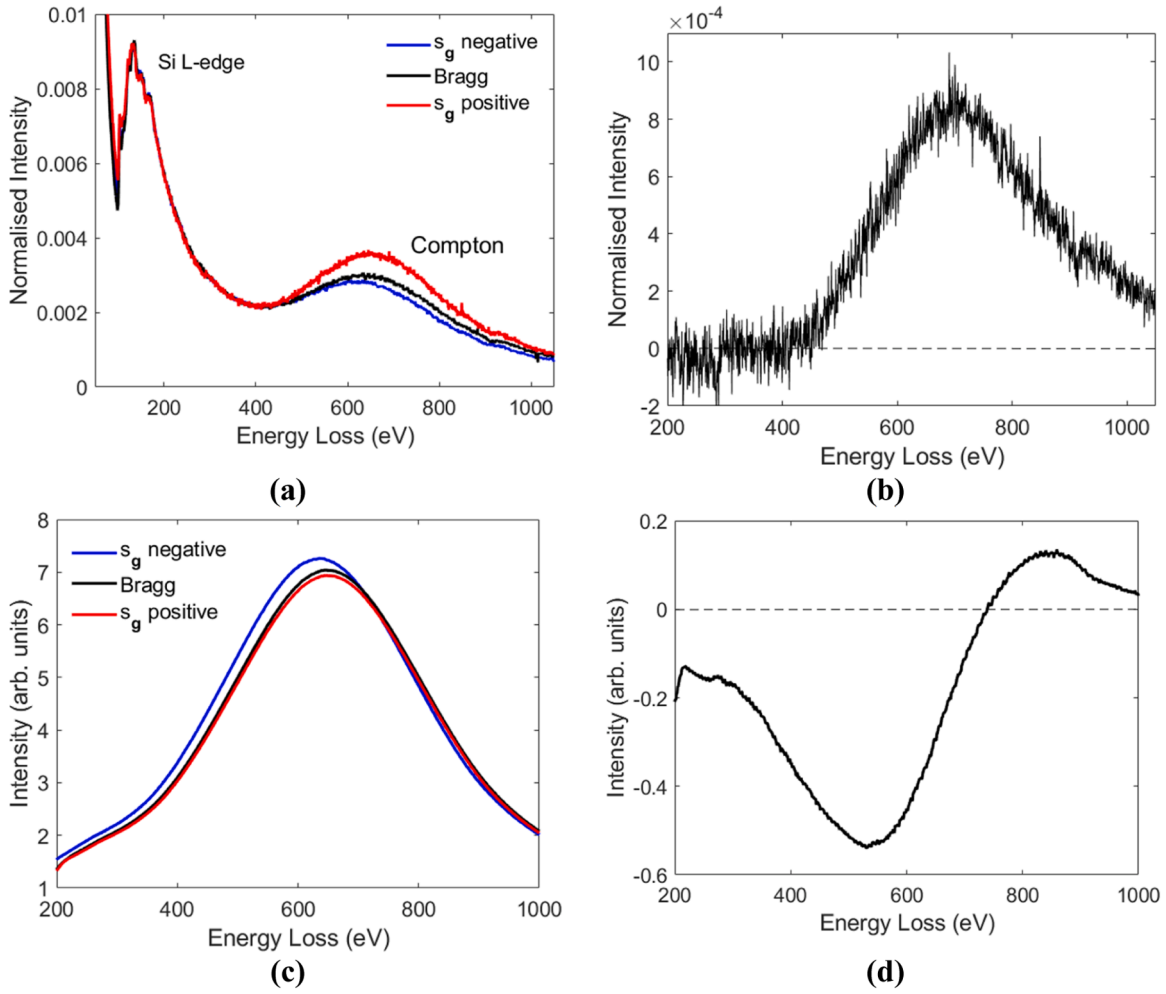

Fig. 3. (a) EELS Compton spectra acquired under 004 two-beam conditions with different deviation parameter (s_g) values. The integrated intensity in the Si L-edge region (i.e. 115–175 eV) is normalised for a direct comparison. (b) Difference spectrum obtained by subtracting the s_g negative from s_g positive spectrum. (c) Multislice simulated Compton spectra for the same experimental conditions. Only direct scattering contributions are modelled. (d) Difference spectrum obtained from the multislice results.

(<1%). Furthermore, the EELS spectrometer is not a point detector, but has a finite (i.e. 5.3 mrad) collection semi-angle, which produces a range of q values that is larger than the changes in deviation parameter. Therefore, the effect of q on direct scattering should be small.

A second consideration is the role of deviation parameter on the 000 and Bragg beam intensities. For an absorbing crystal under two-beam conditions the Bragg beam intensity is symmetrical with respect to deviation parameter, while the 000 beam intensity is higher for positive deviation parameter [26]. This is apparent in Fig. 4a, which is a convergent beam electron diffraction (CBED) pattern for silicon in the 004 two-beam condition, acquired from a specimen region with thickness similar to the Compton measurements (i.e. 70 nm). The 000 beam intensity at negative deviation parameter is smaller than the positive deviation parameter intensity by a factor of 0.86 (the deviation parameters are the same as the Compton measurements). Although non-negligible, the intensity asymmetry is still not large enough to quantitatively explain the observed increase in Compton signal with deviation parameter (Fig. 3a).

To further quantify the role of scattering vector magnitude q and 000/Bragg beam intensity on Compton spectra, multislice simulations were performed for the same conditions as experiment. The simulated Compton spectra at positive and negative deviation parameter, as well as Bragg, are superimposed in Fig. 3c. The simulations only model direct Compton scattering, and therefore do not include interference effects. There is nevertheless good agreement between experiment and simulation at the Bragg orientation, where interference effects are minimal (see discussion below Eq. 26). For example, the Compton peak maximum is at ~663 eV and 653 eV for experiment and simulation respectively. However, changes in the experimentally measured Compton profile with deviation parameter are not reproduced by simulation. For example, with increasing deviation parameter the simulated Compton peak maximum shifts to higher energy loss, consistent with experiment, but the overall intensity decreases (cf. Fig. 3a). Furthermore, the simulated difference spectrum (Fig. 3d) has a very different shape to Fig. 3b, and the integrated (absolute) intensity is only 6% the intensity of the simulated Compton profile at negative deviation parameter, a significantly smaller fraction compared to experiment.

The results suggest that changes in the Compton spectra with deviation parameter are primarily due to coherent scattering from beam interference, rather than direct scattering. The difference spectrum is therefore a direct measure of the non-diagonal terms in the electron momentum density matrix. Assume a crystal in the '2 beams in, 1 beam out' diffraction condition, so that $\mathbf{k}_i$ and $\mathbf{k}_i'$ can take only two values, i.e. incident wavevector for the 000 and Bragg beam, while $\mathbf{k}_e$ and $\mathbf{k}_e'$ are equal to the wavevector of the exit beam. The scattering cross-section (Eq. 16) therefore has only two indirect terms, i.e.:

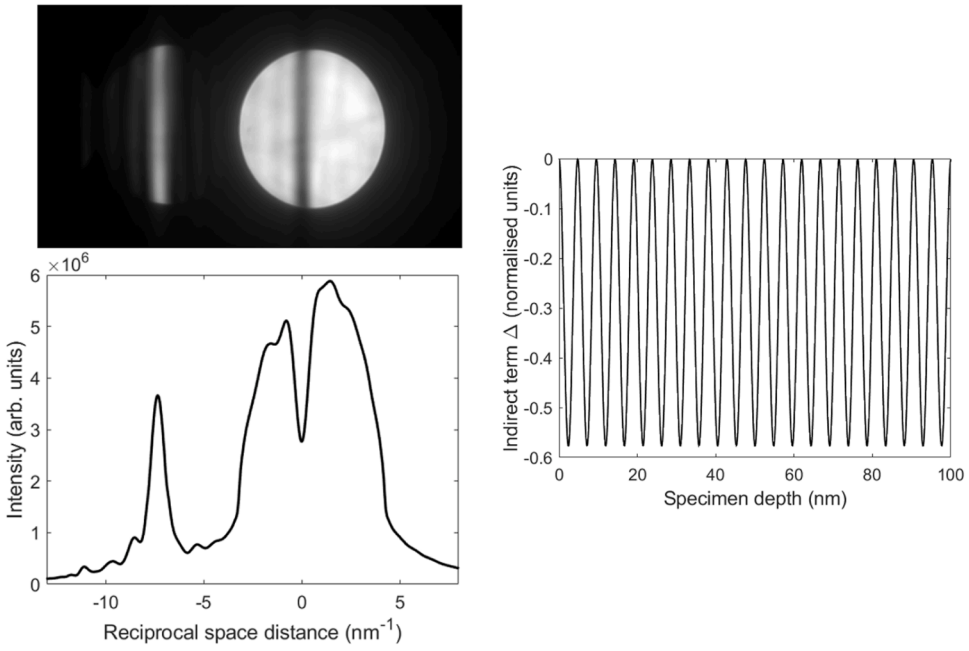

Fig. 4. (a) CBED pattern for silicon in 004 two-beam diffraction conditions and corresponding rocking beam intensity curve. (b) Plot of the indirect scattering contribution Δ to the $\mathbf{g} = 004$ coherent electron Compton signal as a function of specimen depth in silicon. The sample is assumed to be non-absorbing and $|w| = 3.1$. Δ is plotted on a scale where the incident electron beam intensity is normalised to unity.

$$\frac{|\phi_{e\mathbf{0}}|^2\phi_{i\mathbf{g}}^*\phi_{i\mathbf{0}}}{(qq')^2}\left[\sum_{\mathbf{p}''} < i|\mathbf{p}'' + \mathbf{g} >< \mathbf{p}''|i > \delta\left(\hbar\omega - \frac{h^2\left(q^2 - g^2 - 2\mathbf{p}''\cdot\mathbf{q}'\right)}{2m}\right)\right]$$
$$+\frac{|\phi_{e\mathbf{0}}|^2\phi_{i\mathbf{0}}^*\phi_{i\mathbf{g}}}{(qq')^2}\left[\sum_{\mathbf{p}''} < i|\mathbf{p}'' - \mathbf{g} >< \mathbf{p}''|i > \delta\left(\hbar\omega - \frac{h^2\left((q')^2 - g^2 - 2\mathbf{p}''\cdot\mathbf{q}\right)}{2m}\right)\right] \tag{21}$$

where $\phi_{i\mathbf{0}}$, $\phi_{i\mathbf{g}}$ are the amplitudes of the 000 and Bragg beams for the incident illumination and $\phi_{e\mathbf{0}}$ is the amplitude of the exit beam. The amplitudes are evaluated at the Compton scattering depth. The $\mathbf{q}, \mathbf{q}'$ scattering vectors have been swapped between the two terms in Eq. (21), which results in a change in sign for the reciprocal vector $\mathbf{g}$. Consider the special case where $\mathbf{q}$ and $\mathbf{q}'$ are crystallographically equivalent vectors with equal magnitude, i.e. $q = q'$. Examples include $\mathbf{g} = 004$ and $\bar{2}20$ symmetric two-beam scattering in silicon [3]. The symmetry of the scattering vectors must mean that:

$$\sum_{\mathbf{p}''}\langle i|\mathbf{p}'' + \mathbf{g}\rangle\langle\mathbf{p}''|i\rangle\delta\left(\hbar\omega - \frac{h^2(q^2 - g^2 - 2\mathbf{p}''\cdot\mathbf{q}')}{2m}\right)$$
$$= \sum_{\mathbf{p}''}\langle i|\mathbf{p}'' - \mathbf{g}\rangle\langle\mathbf{p}''|i\rangle\delta\left(\hbar\omega - \frac{h^2\left((q')^2 - g^2 - 2\mathbf{p}''\cdot\mathbf{q}\right)}{2m}\right) \tag{22}$$

Therefore, the indirect scattering cross-section (Eq. 21) simplifies to:

$$\frac{2|\phi_{e\mathbf{0}}|^2\mathrm{Re}\left(\phi_{i\mathbf{g}}^*\phi_{i\mathbf{0}}\right)}{(qq')^2}\left[\sum_{\mathbf{p}''}\langle i|\mathbf{p}'' + \mathbf{g}\rangle\langle\mathbf{p}''|i\rangle\delta\left(\hbar\omega - \frac{h^2(q^2 - g^2 - 2\mathbf{p}''\cdot\mathbf{q}')}{2m}\right)\right] \tag{23}$$

where 'Re' denotes the real part of a complex number. The 000 and Bragg beam amplitudes at specimen depth z are given by [26]:

$$\phi_{i\mathbf{0}}(z) = \sum_{m=1}^{2}\varepsilon^{(m)}C_{\mathbf{0}}^{(m)}\exp\left(2\pi i\gamma^{(m)}z\right) \tag{24a}$$

$$\phi_{i\mathbf{g}}(z) = \sum_{m=1}^{2}\varepsilon^{(m)}C_{\mathbf{g}}^{(m)}\exp\left(2\pi i\gamma^{(m)}z\right) \tag{24b}$$

where the $C_{\mathbf{g}}^{(m)}$ terms are Bloch wave coefficients for the incident, high energy electron in the crystal (not to be confused with the Bloch wavefunction for solid-state electrons; Eq. 17). $\varepsilon^{(m)}$ and $\gamma^{(m)}$ are the excitation and change in longitudinal wavevector for the m^{th}-Bloch state. Due to two-beam diffraction conditions there are only two Bloch states for the incident electron, labelled '1' and '2' respectively. For a non-absorbing crystal $\varepsilon^{(m)} = [C_{\mathbf{0}}^{(m)}]^*$ [26], and it is easy to show that (see Supplementary Material):

$$\mathrm{Re}\left(\phi_{i\mathbf{g}}^*\phi_{i\mathbf{0}}\right) =$$
$$= \frac{2\gamma^{(1)}\xi_{\mathbf{g}}}{\left[1 + \left(2\gamma^{(1)}\xi_{\mathbf{g}}\right)^2\right]^2} + \frac{2\gamma^{(2)}\xi_{\mathbf{g}}}{\left[1 + \left(2\gamma^{(2)}\xi_{\mathbf{g}}\right)^2\right]^2}$$
$$+ \frac{2\left(\gamma^{(1)} + \gamma^{(2)}\right)\xi_{\mathbf{g}}\cos[2\pi(\Delta\gamma)z]}{\left[1 + \left(2\gamma^{(1)}\xi_{\mathbf{g}}\right)^2\right]\left[1 + \left(2\gamma^{(2)}\xi_{\mathbf{g}}\right)^2\right]} \tag{25}$$

where $\Delta\gamma = \gamma^{(1)} - \gamma^{(2)}$, and $\xi_{\mathbf{g}}$ is the extinction distance. Furthermore [26]:

$$\gamma^{(1)} = \frac{w + \sqrt{1 + w^2}}{2\xi_{\mathbf{g}}};\ \gamma^{(2)} = \frac{w - \sqrt{1 + w^2}}{2\xi_{\mathbf{g}}} \tag{26}$$

where $w = s_{\mathbf{g}}\xi_{\mathbf{g}}$ is the dimensionless deviation parameter. At the Bragg orientation $w = 0$ and $\gamma^{(1)} = -\gamma^{(2)}$, so that $\mathrm{Re}(\phi_{i\mathbf{g}}^*\phi_{i\mathbf{0}}) = 0$. The Compton profile at Bragg is therefore free from interference effects, a result that has also been derived previously [4]. There will however be an interference contribution for non-zero values of w. Consider two Compton spectra acquired at equal and opposite values of w. Since for a non-absorbing crystal the 000 and Bragg beam intensities are symmetrical with respect to w, the direct terms will cancel one another in a difference spectrum. From Eqs. (25) to (26) however, the indirect terms

will not completely cancel, so that the difference spectrum is proportional to the projected, non-diagonal electron momentum density, i.e. the square bracket term in Eq. (23).

The third term in Eq. (25) indicates that there is an oscillatory depth dependence to the indirect contribution. Fig. 4b plots the indirect contribution Δ in the $\mathbf{g} = 004$ Compton difference spectrum as a function of specimen depth, assuming no absorption and $|w| = 3.1$ (the w-value is similar to the experimental deviation parameters in Fig. 3a). The indirect contribution is defined as $\Delta = [\mathrm{Re}(\phi^*_{\mathbf{ig}}\phi_{\mathbf{i0}})]_{w^+} - [\mathrm{Re}(\phi^*_{\mathbf{ig}}\phi_{\mathbf{i0}})]_{w^-}$, where w^+ and w^- are the positive and negative dimensionless deviation parameters respectively. There are large depth oscillations in Δ between 0 and −0.6 (here the incident electron beam intensity is normalised to unity). For a non-absorbing crystal it can be shown that $\Delta \leq 0$ for $|w^+| = |w^-|$ (see Supplementary Material). Compton scattering can occur at any given depth and therefore the indirect contribution must be integrated over the specimen thickness. Since Δ is always of the same sign its integral can result in an appreciable non-zero value, and consequently a large difference spectrum (e.g. Fig. 3b).

In our measurements the negative and positive deviation parameter had slightly different magnitudes, i.e. $w = -2.7$ and $w = 3.4$ respectively. There will then be a residual intensity in the 000 and Bragg beams while extracting the difference spectrum. Nevertheless, for a non-absorbing crystal it can be shown that the direct scattering contributions from the two beams are out of phase, and therefore cancel one another (see Supplementary Material). The only remaining contribution is the indirect term Δ, which has a less regular depth dependence pendellösung, although the sign remains negative throughout (see Supplementary Material). Fig. 4a indicates that the relative difference in 000 beam intensity for positive and negative deviation parameter is 14%. Therefore, absorption cannot be entirely ruled out in our measurement, although interference is still the dominant contribution to the difference spectrum.

The interference term in the difference spectrum is proportional to the projected, non-diagonal electron momentum density for the solid. From Eq. (23) the measured quantity is given by:

$$\theta(p_z, \mathbf{g}) = \sum_{\mathbf{p}} \chi(\mathbf{p}+\mathbf{g})^* \chi(\mathbf{p}) \delta\left(\hbar\omega - \frac{h^2(q^2 - g^2 - 2p_z q)}{2m}\right) \quad (27)$$

where $\chi(\mathbf{p})$ is the Fourier transform of the solid-state electron wavefunction at reciprocal vector $\mathbf{p}$. p_z is the component of $\mathbf{p}$ along the scattering vector $\mathbf{q}'$ or $\mathbf{q}$ (since $\mathbf{q}$ and $\mathbf{q}'$ are crystallographically equivalent vectors of equal magnitude the exact choice of scattering vector is not important). Eq. (27) reduces to the projected electron momentum density $J(p_z)$ for $\mathbf{g} = 0$. For a periodic crystal the auto-correlation term $\chi(\mathbf{p}+\mathbf{g})^*\chi(\mathbf{p})$ is expected to have maximum amplitude when $\mathbf{p}$ is a null vector. This suggests that $\theta(p_z, \mathbf{g})$ has an extremum (i.e. maximum or minimum) at $p_z = 0$ [12], which corresponds to an energy loss $h^2(q^2 - g^2)/2m$ in the difference spectrum.

Fig. 5a shows $\theta(p_z, \mathbf{g} = 004)$ extracted from the difference spectrum in Fig. 3b using Eq. (27). The sign of $\theta(p_z, \mathbf{g} = 004)$ is made negative, since the difference spectrum also contains a pre-factor due to beam interference (Eq. 23), with negative Δ-values (Fig. 4b). p_z is approximately parallel to the scattering vector $[\bar{3}, 4, 1]$, which was calculated using the method described in [3]. The minimum of $\theta(p_z, \mathbf{g} = 004)$ in Fig. 5a does not coincide with $p_z = 0$. This is also a feature for Compton measurements of $J(p_z)$, and is because the measured EELS spectrum has an additional angular dependence due to Rutherford scattering [28]. This results in the $(qq')^{-2}$ term in Eq. (23), which is a variable over the EELS aperture, and therefore distorts the Compton profile from its ideal shape. In Fig. 5b, $\theta(p_z, \mathbf{g} = 004)$ is replotted with the peak minimum at $p_z = 0$. The graph is asymmetric with respect to p_z, due to the non-zero reciprocal vector $\mathbf{g}$.

$\mathbf{g} = \bar{2}20$, two-beam EELS Compton spectra acquired under Bragg, positive ($s_{\mathbf{g}} = 1.1 \pm 0.1 \times 10^{-2}$ nm^{-1}) and negative ($s_{\mathbf{g}} = -0.8 \pm 0.1 \times 10^{-2}$ nm^{-1}) deviation parameter are shown superimposed in Fig. 6a. The integrated intensity of the Si L-edge region, between 115 and 175 eV, is normalised for a direct comparison. The relative intensity of the Compton signal increases from negative to positive deviation parameter, while the peak maximum shifts to lower energy losses. Exner and Schattschneider [7] however observed a higher Compton signal for negative deviation parameter, although the sense of the peak shift is the same. The reason for the discrepancy is not clear, but may be due to differences in the experimental conditions for the two measurements. In particular, the Compton scattering angle in reference [7] is much larger than the present work, as evidenced by a higher Compton peak maximum between 1200 and 1400 eV (see Fig. 8 in [7]). It should also be noted that the sense of the peak shift is opposite to the $\mathbf{g} = 004$ results (Fig. 3a).

Fig. 6b is the difference spectrum between the positive and negative deviation parameter Compton profiles. The integrated intensity is approximately a third of the background subtracted, negative deviation parameter Compton profile, indicating a large change in the Compton spectrum with deviation parameter. Fig. 6c plots the multislice simulated Compton spectra for the different diffraction conditions. Recall that these simulations model only the direct scattering contributions. The simulations do not reproduce the experimental trends in peak shift or intensity, and the simulated difference spectrum (Fig. 6d) has a very different shape and relative intensity, i.e. the integrated (absolute) intensity is only 4% the intensity of the simulated Compton profile at negative deviation parameter. This indicates that the experimental $\mathbf{g} =$

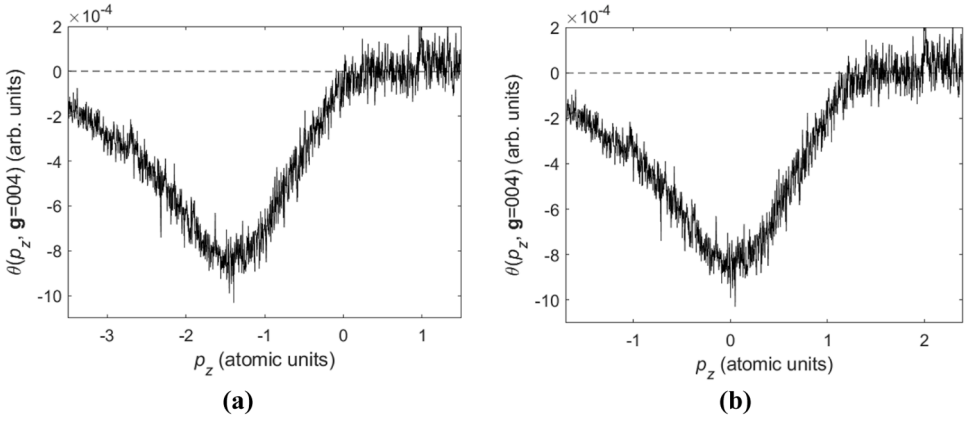

Fig. 5. (a) $\theta(p_z, \mathbf{g} = 004)$ extracted from Fig. 3b, and including the negative sign of the beam interference term Δ. p_z is approximately parallel to the $[\bar{3}, 4, 1]$ scattering vector. (b) The same plot but with the scattering vector magnitude adjusted so that the minimum in $\theta(p_z, \mathbf{g} = 004)$ is at $p_z = 0$.

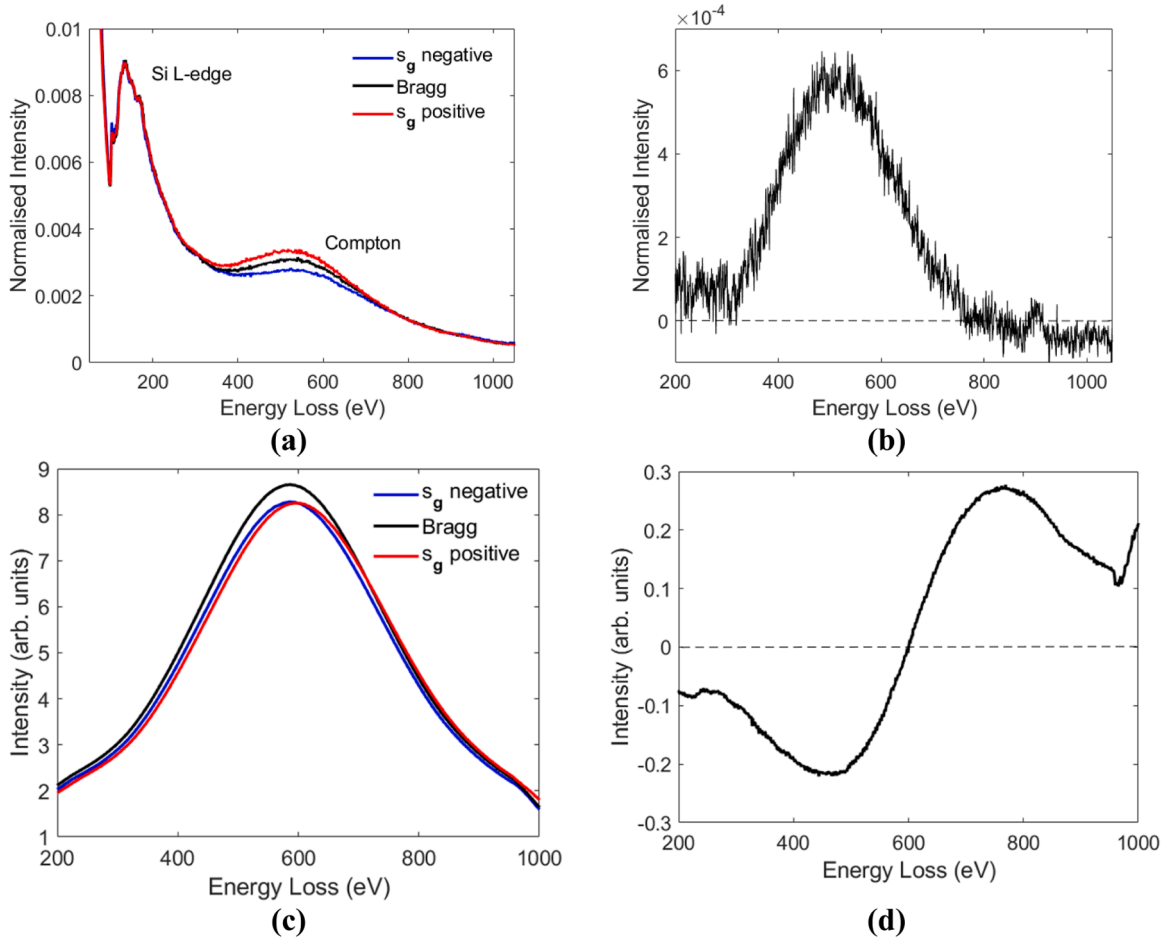

Fig. 6. (a) EELS Compton spectra acquired under $\bar{2}20$ two-beam conditions with different deviation parameter (s_g) values. The integrated intensity in the Si L-edge region (i.e. 115–175 eV) is normalised for a direct comparison. (b) Difference spectrum obtained by subtracting the s_g negative from s_g positive spectrum. (c) Multislice simulated Compton spectra for the same experimental conditions. Only direct scattering contributions are modelled. (d) Difference spectrum obtained from the multislice results.

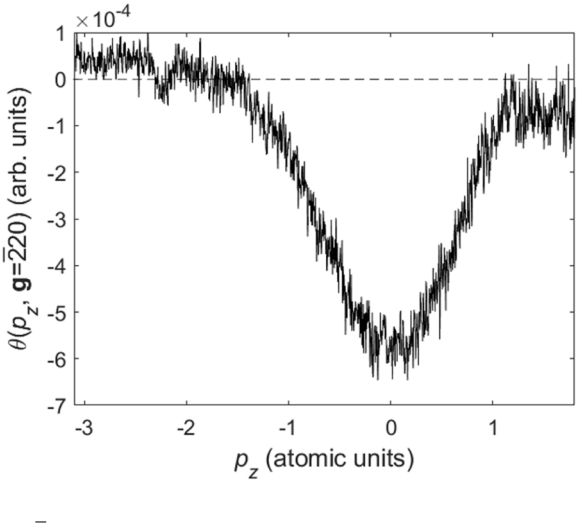

Fig. 7. $\theta(p_z, \mathbf{g} = \bar{2}20\ )$ extracted from Fig. 6b, and including the negative sign of the beam interference term Δ. p_z is approximately parallel to the $[\bar{1},\ 0,\ \bar{5}]$ scattering vector. The scattering vector magnitude is adjusted so that the minimum in $\theta(p_z, \mathbf{g} = \bar{2}20\ )$ is at $p_z = 0$.

$\bar{2}20$ difference spectrum is largely due to beam interference. $\theta(p_z, \mathbf{g} = \bar{2}20\ )$ is shown in Fig. 7, after correcting for the negative sign of Δ. p_z is approximately parallel to the scattering vector $[\bar{1},\ 0,\ \bar{5}]$, and the scattering vector magnitude has been adjusted so that the peak minimum is at $p_z = 0$. The range of $\theta(p_z, \mathbf{g} = \bar{2}20\ )$, i.e. $p_z \approx \pm 1$ atomic units, is much smaller than $J(p_z)$; see, for example, Fig. 3d in [11]. This is presumably because the auto-correlation term $\chi(\mathbf{p}+\mathbf{g})^*\chi(\mathbf{p})$ decays more rapidly with p_z when $\mathbf{g} \neq \mathbf{0}$.

5. Summary

Compton EELS spectra are acquired for $\mathbf{g} = 004$ and $\bar{2}20$ two-beam conditions in silicon with both positive and negative deviation parameter. Multislice simulations confirm that direct Compton scattering of the 000 and Bragg beams has only a small contribution to the difference spectrum. Therefore, interference between the two beams, i.e. coherent Compton scattering, must be the dominant contribution. Dynamical electron diffraction theory is used to analyse the variation of the coherent Compton signal as a function of specimen depth. Despite the oscillation of 000 and Bragg beam amplitudes the coherent Compton scattering at each depth in a non-absorbing crystal will always add cumulatively. Therefore, the measured coherent Compton signal can be quite large for a specimen of reasonable thickness, consistent with our experimental results. The difference spectrum is used to extract $\theta(p_z, \mathbf{g})$, the projected, non-diagonal electron momentum density for the solid. Experimental $\theta(p_z, \mathbf{g})$ curves for silicon are asymmetrical and generally

narrower compared to the projected electron momentum density $J(p_z)$ obtained from a standard Compton measurement. These observations are consistent with the auto-correlation of the Fourier transformed electron wavefunction, i.e. $\chi(\mathbf{p}+\mathbf{g})^*\chi(\mathbf{p})$, from which $\theta(p_z,\mathbf{g})$ is derived.

Declaration of Competing Interest

The authors declare that they have no known competing financial interests or personal relationships that could have appeared to influence the work reported in this paper.

Data availability

Data will be made available on request.

Supplementary materials

Supplementary material associated with this article can be found, in the online version, at doi:10.1016/j.ultramic.2022.113664.

References

[1] MJ Cooper, PE Mijnarends, N Shiotani, N Sakai, A Bansil, X-Ray ComptonScattering, Oxford University Press, Oxford, 2004.
[2] BG Williams, TG Sparrow, RF Egerton, Electron Compton scattering of solids, Proc. R. Soc. Lond. A 393 (1984) 409–422.
[3] P Jonas, P Schattschneider, Electron Compton scattering in a symmetric two-beam scattering geometry, Microsc. Microanal. Microstruct. 4 (1993) 63–85.
[4] A Exner, H Kohl, P & Schattschneider, P Jonas, Coherent electron Compton scattering in crystals, J. Phys.: Condens. Matter 6 (1994) 3443–3452.
[5] A Exner, P Schattschneider, IE McCarthy, Compton profiles from amorphous allotropes of carbon, Micron 27 (1996) 1–9.
[6] A Exner, H Kohl, M Nelhiebel, P Schattschneider, Interference in electron Compton scattering for silicon, J. Phys.: Condens. Matter 8 (1996) 2835–2850.
[7] A Exner, P Schattschneider, Asymmetries in electron Compton profiles of silicon- a coherence effect, Ultramicroscopy 65 (1996) 131–145.
[8] Z Feng, S Löffler, F Eder, D Su, JC Meyer, P Schattschneider, Combined study of the ground and unoccupied electronic states of graphite by electron energy-loss spectroscopy, J. Appl. Phys. 114 (2013), 183716, 8 pages.
[9] Z Feng, X Zhang, Y Sakurai, Z Wang, H Li, H Hu, Compton profile of few-layer graphene investigated by electron energy-loss spectroscopy, Sci. Rep. 9 (2019), 17313, https://doi.org/10.1038/s41598-019-53928-2.
[10] A Talmantaite, MRC Hunt, BG Mendis, Electron Compton scattering and the measurement of electron momentum distribution in solids, J. Microsc. 279 (2020) 185–188.
[11] BG Mendis, A talmantaite, towards electron energy loss compton spectra free from dynamical diffraction artefacts, Microsc. Microanal. 28 (2022) 1971–1980.
[12] W Schülke, S Mourikis, Nondiagonal momentum density of Si by coherent X-ray scattering, Acta Cryst. A 42 (1986) 86–98.
[13] H & Kohl, H Rose, Theory of image formation by inelastically scattered electrons in the electron microscope, Adv. Electron. Electron Phys. 65 (1985) 173–227.
[14] P Schattschneider, M Nelhiebel, H Souchay, B Jouffrey, The physical significance of the mixed dynamic form factor, Micron 31 (2000) 333–345.
[15] LJ Allen, AJ D'Alfonso, SD Findlay, Modelling the inelastic scattering of fast electrons, Ultramicroscopy 151 (2015) 11–22.
[16] P Schattschneider, S Rubino, C Hébert, J Rusz, J Kuneš, P Novák, E Carlino, M Fabrizioli, G Panaccione, G Rossi, Detection of magnetic circular dichroism using a transmission electron microscope, Nature 441 (2006) 486–488.
[17] S Löffler, V Motsch, P Schattschneider, A pure state decomposition approach of the mixed dynamic form factor for mapping atomic orbitals, Ultramicroscopy 131 (2013) 39–45.
[18] K Ishizuka, Multislice formula for inclined illumination, Acta Cryst. A 38 (1982) 773–779.
[19] Y Kainuma, The theory of Kikuchi patterns, Acta Cryst 8 (1955) 247–257.
[20] EJ Kirkland, Advanced Computing in Electron Microscopy, 2nd Edition, Springer, New York, 2010.
[21] P Schattschneider, P Pongratz, H Hohenegger, Compton scattering in electron energy loss spectroscopy, Scann. Microsc. 4 (1990) 35–43.
[22] P Schattschneider, Fundamentals of Inelastic Electron Scattering, Springer-Verlag, Vienna, 1986.
[23] P Eisenberger, PM Platzman, Compton scattering of X rays from bound electrons, Phys. Rev. A 2 (1970) 415–423.
[24] BG Mendis, QM Ramasse, Removal of core hole distortion from ionization edges in electron energy loss spectroscopy, Phys. Rev. B 103 (2021), 205102, 11 pages.
[25] NW Ashcroft, N.D. Mermin ND, Solid State Physics, Holt, Rinehart and Winston, USA, 1976.
[26] PB Hirsch, A Howie, RB Nicholson, DW Pashley, MJ Whelan, Electron Microscopy of Thin Crystals, Butterworths, Great Britain, 1965.
[27] JCH Spence, JM Zuo, Electron Microdiffraction, Plenum Press, New York, 1992.
[28] DS Su, P Jonas, P Schattschneider, The multiple-scattering problem in electron Compton scattering on solids, Phil. Mag. B 66 (1992) 405–418.